

# A Fast Hybrid Field-Circuit Simulator for Transient Analysis of Microwave Circuits

Kemal Aygün, Brian C. Fischer, Jun Meng, Balasubramaniam Shanker, *Senior Member, IEEE*, and Eric Michielssen, *Fellow, IEEE*

**Abstract**—A plane-wave-time-domain accelerated time-domain integral-equation solver is coupled to a SPICE-like transient circuit simulator to analyze electromagnetic platform-circuit interactions. The hybrid field-circuit simulator simultaneously solves surface-wire-volume time-domain integral equations that model electromagnetic interactions with the platform and modified nodal analysis equations that govern the behavior of the potentially nonlinear lumped circuits. A shielded nonlinear microwave amplifier is analyzed using the proposed scheme, and its immunity to electromagnetic interference is assessed.

**Index Terms**—Electromagnetic interference (EMI), integral equations, marching on in time (MOT), nonlinear circuits, plane-wave time domain (PWTD).

## I. INTRODUCTION

IN THIS paper, a SPICE-like transient circuit simulator is integrated into a time-domain integral equation (TDIE) solver to accomplish the fast and accurate simulation of complex microwave structures loaded with linear and nonlinear lumped circuits of arbitrary topology. Methods to account for lumped circuit loads in full-wave electromagnetic simulators have been studied extensively in the literature. Here, the focus is on time-domain methods, which we believe to be better suited for tackling broad-band/nonlinear problems than their frequency-domain counterparts.

Earlier attempts to analyze electromagnetic wave interactions with structures containing lumped circuit loads using full-wave time-domain field solvers mostly leveraged differential equation methods. For example, in the finite-difference time-domain (FDTD) method, lumped circuits are included by either distributing them into the FDTD grid (lumped-element method [1]–[3]) or by introducing an equivalent circuit model at specific FDTD grid edges (equivalent source method [4]–[6]). These techniques have been applied to problems ranging from high-speed interconnects [7], [8] to active microwave circuits [9], [10]. Similar methods have been used to model lumped circuits within the framework of transmission-line method solvers

[11]. Recently, the finite-element time-domain (FETD) method has been extended to model interactions between lumped circuits and the platforms they are mounted on using an approach that bears similarities to the FDTD equivalent source method [12]–[14].

Initially, TDIE methods that account for the presence of lumped circuits focused mainly on thin-wire structures. In [15], dipole and square loop antennas with simple linear and piecewise-linear loads are analyzed using the Norton convolution integral approach. Wire-frame networks with nonlinear loads are considered in [16], where the circuit nodal equations are coupled to integral equations by representing the wire geometries by Norton equivalent circuits. The treatment of arbitrary passive lumped circuits was introduced in [17] by applying trapezoidal integration to the branch constitutive relations for inductors and capacitors. However, this method is restricted to circuits containing resistors, inductors, and capacitors and, furthermore, requires explicit derivations of the equivalent circuits for arbitrary *RLC* configurations. The coupled electromagnetic and circuit simulation of perfect electrically conducting (PEC) surfaces via a TDIE formulation was previously introduced using the partial-element equivalent-circuit (PEEC) approach. The classical PEEC scheme [18] models conductor cross sections as volumetric filaments of rectangular cross section. The full-wave interactions between these filaments are then represented in terms of equivalent inductance, capacitance, and resistance matrices and can be ported to a circuit simulator. The PEEC-based transient modeling of noise interactions in PEC interconnect systems was presented in [19] and [20]. A surface-based formulation of the PEEC method including modeling of skin-effect was demonstrated first in the frequency domain [21], and more recently in the time domain [22].

Historically, the development of TDIE methods has lagged behind that of the FDTD/FETD methods as TDIE schemes were found to be prone to late-time instabilities and were computationally expensive. Recently, however, noticeable progress has been made toward the stabilization of both PEEC and marching-on-in-time (MOT) algorithms for solving TDIEs [23]–[25]. In addition, the introduction of the plane-wave-time-domain (PWTD) algorithm has considerably reduced the computational complexity of classical MOT solvers [26], [27]. In this study, a SPICE-like transient nonlinear circuit simulator (complete with SPICE-equivalent device models) is incorporated into a PWTD-accelerated MOT-based TDIE solver to create a fast hybrid field-circuit simulator which allows lumped circuits and the platforms that they are mounted on to be analyzed simultaneously in a consistent and efficient manner. The PWTD acceleration of the hybrid field-circuit solver along with the modeling capability of microwave geome-

Manuscript received May 7, 2003; revised September 8, 2003.

K. Aygün was with the Center for Computational Electromagnetics, Department of Electrical and Computer Engineering, University of Illinois at Urbana-Champaign, Urbana, IL 61801 USA. He is now with the Intel Corporation, Chandler, AZ 85226 USA.

B. C. Fischer is with Lockheed Martin Space and Strategic Missiles, Sunnyvale, CA 94088 USA.

J. Meng and E. Michielssen are with the Center for Computational Electromagnetics, Department of Electrical and Computer Engineering, University of Illinois at Urbana-Champaign, Urbana, IL 61801 USA.

B. Shanker is with the Department of Electrical and Computer Engineering, Michigan State University, East Lansing, MI 48824 USA.

Digital Object Identifier 10.1109/TMTT.2003.821929

tries composed of arbitrarily shaped PEC surfaces/wires and finite/ (possibly) inhomogeneous dielectrics utilizing a stable and robust MOT formulation constitute the main contributions of this paper.

The proposed solver is detailed in Section II and thereafter applied to the analysis of a shielded nonlinear active microwave amplifier subject to electromagnetic interference (EMI) from external sources. The conclusions of this study are stated in Section IV.

## II. FORMULATION

This section first describes a PWTD-accelerated MOT-based TDIE solver that permits analyzing microwave structures composed of both PEC surfaces/wires and inhomogeneous dielectric volumes. This solver is constructed so that it can be easily coupled to the SPICE-like transient circuit simulator that is described next. The details of the coupling scheme are also elucidated.

### A. Construction of the MOT-PWTD Algorithm

A comprehensive description of the multilevel PWTD algorithm and the application of a two-level PWTD accelerated MOT scheme to the analysis of electromagnetic compatibility (EMC)/EMI phenomena involving PEC structures were reported in [26] and [28], respectively. Incorporation of dielectric materials into the multilevel PWTD scheme was detailed in [29]. Here a succinct outline of the MOT-PWTD scheme is presented to allow for a description of the hybrid field-circuit solver.

The PEC features of the microwave structures considered herein are denoted by  $S$  and may comprise surfaces, wires, and surface-wire junctions. Dielectric elements occupy volume  $V$  and are to be assumed isotropic and nonmagnetic and of frequency-independent permittivity  $\varepsilon(\mathbf{r})$ . An electric field  $\mathbf{E}^i(\mathbf{r}, t)$  that is (approximately) temporally band-limited to  $f_{\max}$  and that (approximately) vanishes for  $t < 0$  excites  $S \cup V$  and induces surface currents  $\mathbf{J}^s(\mathbf{r}, t)$  on  $S$  and volumetric polarization currents  $\mathbf{J}^v(\mathbf{r}, t)$  in  $V$ . Currents  $\mathbf{J}^s(\mathbf{r}, t)$  and  $\mathbf{J}^v(\mathbf{r}, t)$  radiate scattered electric fields  $\mathbf{E}^{\text{sca}}(\mathbf{r}, t, \mathbf{J}^s)$  and  $\mathbf{E}^{\text{sca}}(\mathbf{r}, t, \mathbf{J}^v)$ , respectively. The total electric field is  $\mathbf{E}^{\text{tot}}(\mathbf{r}, t) = \mathbf{E}^i(\mathbf{r}, t) + \mathbf{E}^{\text{sca}}(\mathbf{r}, t, \mathbf{J}^s) + \mathbf{E}^{\text{sca}}(\mathbf{r}, t, \mathbf{J}^v)$ . The dielectric polarization currents  $\mathbf{J}^v(\mathbf{r}, t)$  are related to the displacement vector  $\mathbf{D}^{\text{tot}}(\mathbf{r}, t) = \varepsilon(\mathbf{r})\mathbf{E}^{\text{tot}}(\mathbf{r}, t)$  as  $\mathbf{J}^v(\mathbf{r}, t) = \kappa(r)\partial_t\mathbf{D}^{\text{tot}}(\mathbf{r}, t)$ , where  $\partial_t$  denotes a temporal derivative and  $\kappa(\mathbf{r}) = (\varepsilon(\mathbf{r}) - \varepsilon_0)/\varepsilon(\mathbf{r})$  is the contrast ratio. A set of coupled integral equations in terms of the unknowns  $\mathbf{J}^s(\mathbf{r}, t)$  and  $\mathbf{D}^{\text{tot}}(\mathbf{r}, t)$  is constructed that enforce the boundary condition for the electric field on  $S$  and a consistency condition between electric field constituents within  $V$  and is given as follows:

$$\hat{n} \times \hat{n} \times \partial_t \mathbf{E}^{\text{tot}}(\mathbf{r}, t) = 0, \quad \mathbf{r} \in S \quad (1)$$

$$\begin{aligned} \partial_t \mathbf{E}^{\text{tot}}(\mathbf{r}, t) &= \partial_t \mathbf{E}^i(\mathbf{r}, t) + \partial_t \mathbf{E}^{\text{sca}}(\mathbf{r}, t, \mathbf{J}^s) \\ &\quad + \partial_t \mathbf{E}^{\text{sca}}(\mathbf{r}, t, \mathbf{J}^v), \quad \mathbf{r} \in V. \end{aligned} \quad (2)$$

Here,  $\hat{n}$  is an outward pointing normal to  $S$  as

$$\begin{aligned} \partial_t \mathbf{E}^{\text{sca}}(\mathbf{r}, t, \mathbf{J}^q) &= -\frac{\mu_0}{4\pi} \int_{\xi} d\xi (\partial_t^2 I - c^2 \nabla \nabla) \\ &\quad \cdot \frac{\mathbf{J}^q(\mathbf{r}', t - \frac{R}{c_0})}{R} \end{aligned} \quad (3)$$

where  $\xi = (S, V)$  for  $q = (s, v)$ ,  $c_0 = 1/\sqrt{\mu_0\varepsilon_0}$  is the free-space speed of light, and  $R = |\mathbf{r} - \mathbf{r}'|$ .

To solve (1) and (2),  $\mathbf{J}^s(\mathbf{r}, t)$  and  $\mathbf{D}^{\text{tot}}(\mathbf{r}, t)$  are expanded in space-time basis functions as

$$\begin{aligned} \mathbf{J}^s(\mathbf{r}, t) &= \sum_{n=1}^{N_s} \sum_{j=1}^{N_t} I_{n,j}^s \mathbf{f}_n^s(\mathbf{r}) T_j(t) \\ &= \sum_{n=1}^{N_s} \mathbf{J}_n^s(\mathbf{r}, t) \\ &= \sum_{n=1}^{N_s} \mathbf{f}_n^s(\mathbf{r}) g_n^s(t), \\ \mathbf{D}^{\text{tot}}(\mathbf{r}, t) &= \sum_{n=1}^{N_v} \sum_{j=1}^{N_t} I_{n,j}^v \mathbf{f}_n^v(\mathbf{r}) T_j(t) \\ &= \sum_{n=1}^{N_v} \mathbf{D}_n^{\text{tot}}(\mathbf{r}, t) \\ &= \sum_{n=1}^{N_v} \mathbf{f}_n^v(\mathbf{r}) g_n^v(t), \end{aligned} \quad (4)$$

where  $I_{n,j}^q$  are the unknown weights associated with the space-time basis functions  $\mathbf{f}_n^q(\mathbf{r})T_j(t)$ ,  $q = s, w, sw, d$  (i.e., surface, wire, surface-wire junction, or dielectric),  $T_j(t) = T(t - j\Delta t)$ , and  $\Delta t$  is the time step size. The quantities  $g_n^s(t)$  and  $g_n^v(t)$  will be used later. All basis functions  $\mathbf{f}_n^q(\mathbf{r})T_j(t)$  are detailed in [28]–[30]; for the discussion that follows, it is only important to note that the surface and wire basis functions are normalized and carry a total current of 1 A across the triangle edge or wire node on which they are defined. Substituting (4) into (1) and (2), Galerkin testing the resulting equations in space with  $\mathbf{f}_n^q(\mathbf{r})$ , and point matching at time  $t_j = j\Delta t$ , yields a set of equations that can be cast in matrix form as

$$\mathcal{Z}_0 \mathcal{I}_j = \mathcal{F}_j - \sum_{i=1}^{j-1} \mathcal{Z}_i \mathcal{I}_{j-i} \quad (5)$$

where  $\mathcal{I}_j = [I_{1,j}^s, \dots, I_{N_s,j}^s, I_{1,j}^v, \dots, I_{N_v,j}^v]^T$  and

$$\mathcal{F}_j = \begin{bmatrix} \langle \mathbf{f}_1^s(\mathbf{r}, t), \hat{n} \times \hat{n} \times \partial_t \mathbf{E}^i(\mathbf{r}, t) \rangle \\ \vdots \\ \langle \mathbf{f}_{N_s}^s(\mathbf{r}, t), \hat{n} \times \hat{n} \times \partial_t \mathbf{E}^i(\mathbf{r}, t) \rangle \\ \langle \mathbf{f}_1^v(\mathbf{r}, t), \partial_t \mathbf{E}^i(\mathbf{r}, t) \rangle \\ \vdots \\ \langle \mathbf{f}_{N_v}^v(\mathbf{r}, t), \partial_t \mathbf{E}^i(\mathbf{r}, t) \rangle \end{bmatrix}_{t=t_j} \quad (6)$$

$$\mathcal{Z}_i = \begin{bmatrix} \mathcal{Z}_i^{ss} & \mathcal{Z}_i^{sv} \\ \mathcal{Z}_i^{vs} & \mathcal{Z}_i^{vv} \end{bmatrix}$$

$$\mathcal{Z}_{i,mn}^{ss} = \langle \mathbf{f}_m^s(\mathbf{r}, t), -\hat{n} \times \hat{n} \times \partial_t \mathbf{E}_{n,-i}^{\text{sca},s} \rangle_{t=0}$$

$$\mathcal{Z}_{i,mn}^{sv} = \langle \mathbf{f}_m^s(\mathbf{r}, t), -\hat{n} \times \hat{n} \times \partial_t \mathbf{E}_{n,-i}^{\text{sca},v} \rangle_{t=0}$$

$$\mathcal{Z}_{i,mn}^{vs} = \langle \mathbf{f}_m^v(\mathbf{r}, t), -\partial_t \mathbf{E}_{n,-i}^{\text{sca},s} \rangle_{t=0}$$

$$\mathcal{Z}_{i,mn}^{vv} = \langle \mathbf{f}_m^v(\mathbf{r}, t), \partial_t \mathbf{E}^{\text{tot}}(\mathbf{r}, t) - \partial_t \mathbf{E}_{n,-i}^{\text{sca},v} \rangle_{t=0}. \quad (7)$$

Here,  $\mathbf{E}_{n,-i}^{\text{sca},q} = \mathbf{E}^{\text{sca}}(\mathbf{r}, t, \mathbf{f}_n^q(\mathbf{r})T(t + i\Delta t))$  and  $\langle \cdot, \cdot \rangle$  denotes the standard inner product. (The above equations do not accurately reflect the one-dimensional nature of the wire basis functions—see [30].) The MOT algorithm assumes relaxed initial

conditions and updates  $\mathcal{I}_j$  for each time step by solving (5) using an iterative solver. The main contributor to the computational complexity of the above scheme is the evaluation of the summation on the right-hand side (RHS) of (5), which requires  $O(N_t N_{sv}^2)$  operations [28], where  $N_{sv} = N_s + N_v$ . The recently introduced multilevel PWTD algorithm [26], [27] considerably reduces this computational cost.

To implement a  $N_l$ -level PWTD algorithm within the framework of the MOT scheme,  $S \cup V$  is enclosed within a cubical box. This box is recursively subdivided into eight child boxes a total of  $N_l - 1$  times;  $N_l$  is selected such that the linear dimensions of the smallest box thus generated are approximately  $0.2 \lambda_{\min}$ , where  $\lambda_{\min}$  is the free-space wavelength at frequency  $f_{\max}$ . Next, starting at the coarsest level, all same-level pairs of nonempty boxes are classified as near- or far-field in nature. Two same-level nonempty boxes are said to form a far-field pair if their distance is greater than their linear dimensions *and* if their parent boxes form a near-field pair. Same-level pairs of nonempty boxes that do not constitute a far-field pair are classified as near-field in nature. The interactions between basis functions in near-field boxes are evaluated directly, which costs  $O(N_t N_{sv})$  operations. The interactions between pairs of far-field boxes ( $\alpha_s, \alpha_0$ ), the centers of which are denoted by  $\mathbf{r}_s^c$  and  $\mathbf{r}_0^c$ , are calculated by the PWTD algorithm. First, for all  $\mathbf{f}_n^s(\mathbf{r})$ ,  $n \in \alpha_s$ , temporal source signatures are subdivided into  $L$  consecutive subsignals of duration  $T_s = T/L$  as

$$\begin{aligned} \mathbf{J}_n^s(\mathbf{r}, t) &= \sum_{l=1}^L \mathbf{J}_{n,l}^s(\mathbf{r}, t) = \sum_{l=1}^L \mathbf{f}_n^s(\mathbf{r}) g_{n,l}^s(t) \\ \mathbf{D}_n^{\text{tot}}(\mathbf{r}, t) &= \sum_{l=1}^L \mathbf{D}_{n,l}^{\text{tot}}(\mathbf{r}) = \sum_{l=1}^L \mathbf{f}_n^v(\mathbf{r}) g_{n,l}^v(t). \end{aligned} \quad (8)$$

The field radiated by  $\mathbf{J}_{n,l}^s(\mathbf{r}, t)$  and  $\mathbf{D}_{n,l}^{\text{tot}}(\mathbf{r})$  can then be reconstructed at  $\mathbf{f}_m^q(\mathbf{r})$   $m \in \alpha_0$  using

$$\begin{aligned} &\int_{\xi} d\mathbf{r} \mathbf{f}_m^q(\mathbf{r}) \cdot \partial_t \mathbf{E}^{\text{sca}}(\mathbf{r}, t, \mathbf{J}_{n,l}^q) \\ &= \int_0^{2\pi} d\phi \int_0^{\pi} d\theta \sin \theta \mathcal{S}_m^-(\hat{\mathbf{k}}, t)^T \\ &\quad * \mathcal{T}(\hat{\mathbf{k}}, \mathbf{R}_c, t) * \left[ \mathcal{S}_n^{+,s}(\hat{\mathbf{k}}, t) * g_{n,l}^s(t) + \mathcal{S}_n^{+,v}(\hat{\mathbf{k}}, t) * g_{n,l}^v(t) \right] \end{aligned} \quad (9)$$

for  $t > lT_s$  provided that the closest distance between the two boxes is greater than  $cT_s$  [26]. It is apparent from this criterion that fields reach the observer after  $g_{n,l}^q(t) = 0$  (equivalently, the current has ceased to radiate). In the above equation

$$\mathcal{T}(\hat{\mathbf{k}}, \mathbf{R}_c, t) = \frac{\mu_0}{8\pi^2 c} \partial_t^3 \delta \left[ t - \hat{\mathbf{k}} \cdot \frac{\mathbf{R}_c}{c} \right] \quad (10)$$

is the translation function and

$$\begin{aligned} \mathcal{S}_m^-(\hat{\mathbf{k}}, t) &= \int_{\xi} d\xi \hat{\mathbf{k}} \times \mathbf{f}_m^q(\mathbf{r}) \delta \left[ t - \hat{\mathbf{k}} \cdot \frac{(\mathbf{r} - \mathbf{r}_0^c)}{c} \right] \\ \mathcal{S}_n^{+,v}(\hat{\mathbf{k}}, t) &= \partial_t \int_V dv \kappa(\mathbf{r}) \hat{\mathbf{k}} \\ &\quad \times \mathbf{f}_n^v(\mathbf{r}) \delta \left[ t + \hat{\mathbf{k}} \cdot \frac{(\mathbf{r} - \mathbf{r}_s^c)}{c} \right] \\ \mathcal{S}_n^{+,s}(\hat{\mathbf{k}}, t) &= \int_S ds \hat{\mathbf{k}} \times \mathbf{f}_n^s(\mathbf{r}) \delta \left[ t + \hat{\mathbf{k}} \cdot \frac{(\mathbf{r} - \mathbf{r}_s^c)}{c} \right] \end{aligned} \quad (11)$$

are the projection operators,  $\hat{\mathbf{k}} = \hat{\mathbf{x}} \sin \theta \cos \phi + \hat{\mathbf{y}} \sin \theta \sin \phi + \hat{\mathbf{z}} \cos \theta$ , and  $\mathbf{R}_c = \mathbf{r}_0^c - \mathbf{r}_s^c$ . The spectral integral in (9) is evaluated numerically using appropriate Gaussian quadrature rules, which implies casting this equation as a summation over a discrete set of plane waves. Explicit formulas for the number of plane waves to be used, the appropriate weights, and ray directions may be found in [31]. To evaluate contributions to the RHS of (5) arising from basis functions that reside in the finest level far-field pairs, the MOT-PWTD scheme proceeds in three stages, which are: 1) compute  $\mathcal{S}_n^{+,s}(\hat{\mathbf{k}}, t) * g_{n,l}^s(t) + \mathcal{S}_n^{+,v}(\hat{\mathbf{k}}, t) * g_{n,l}^v(t)$  (outgoing rays) for all finest level boxes; 2) use the translation function defined in (10) to map the outgoing ray data of a source finest level boxes onto the incoming ray data of finest level observer boxes; and 3) map the incoming ray data onto the observer by convolving with  $\mathcal{S}_m^-(\hat{\mathbf{k}}, t)$ . Contributions to the RHS of (5) arising from basis functions that reside in other far-field pairs are obtained by repeating sequence 1)–3) for all levels using interpolation, splicing, anterpolation, and resectioning operators described in [26] and [31].

Using arguments similar to those presented in [26], it can be rigorously shown that the computational complexity of the MOT-PWTD solver scales as  $O(N_t N_{sv})$  if the PEC surfaces and wires are embedded in a dielectric-filled cubical volume  $V$ . However, when analyzing microwave structures with thin and virtually planar (PEC surface bound) dielectric substrates, the computational complexity scales as  $O(N_t N_{sv} \log^2 N_{sv})$  [29].

### B. Modified Nodal Analysis (MNA) Circuit Equations

The circuit simulator used in this study is SPICE2-based [32], [33] and performs linear and nonlinear large-signal transient analysis on an arbitrary number of independent networks containing resistors, inductors, capacitors, dependent/independent voltage and current sources, diodes, bipolar junction transistors, metal–oxide–semiconductor field-effect transistors (MOSFETs), and metal–semiconductor field-effect transistors (MESFETs). Circuit equations are formulated from the circuit topology via MNA [34]. For a circuit composed of linear resistors and independent current and voltage sources, MNA yields

$$\mathcal{Y} \mathcal{V}_j = \mathcal{J}_j \quad (12)$$

at time  $t_j = j\Delta t$ , where  $\mathcal{Y}$  is the time-independent conductance matrix,  $\mathcal{V}_j$  is the vector of unknowns containing both node voltages and voltage source branch currents, and  $\mathcal{J}_j$  is a vector containing the independent source contributions. The overall dimension of the system  $N_c$  is equal to the number of nonreference nodes plus the number of independent voltage sources in the circuit. If there are nonlinear circuit elements, (12) can be extended to

$$\mathcal{Y} \mathcal{V}_j + \mathcal{Y}_j^{nl}(\mathcal{V}_j) = \mathcal{J}_j + \mathcal{J}_j^{nl}(\mathcal{V}_j) \quad (13)$$

where  $\mathcal{Y}_j^{nl}(\mathcal{V}_j)$  and  $\mathcal{J}_j^{nl}(\mathcal{V}_j)$  represent the nonlinear contributions to the left-hand side (LHS) and RHS of (12), respectively. The number of nonlinear equations in (13) is proportional to the number of nonlinear circuit elements. The resulting MNA system of equations is iteratively solved at each time step using either an iterative solver (such as the transpose-free quasi-minimal-residual (TFQMR) algorithm [35]) (in the case of purely

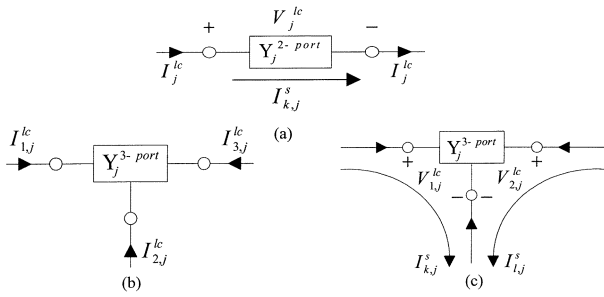


Fig. 1. (a) General two-port lumped circuit defined by a single basis function, (b) general three-port lumped circuit, and (c) three-port lumped circuit defined by two basis functions.

linear circuits) or the multidimensional Newton's method [36] (if there are nonlinear elements in the circuit). The simultaneous solution of the linear and nonlinear equations in (13) is described in more detail in the next subsection, within the context of their coupling to the equations resulting from the electromagnetic field solver. Further details regarding the construction of (12) and (13) for all types of circuit elements considered here can be found in [37].

### C. Hybridization of the MOT-PWTD and MNA Solvers

This section elucidates the hybridization of the above-described MOT-PWTD and MNA solvers. For illustrative purposes, only two- and three-port circuits are considered. However, generalization of the proposed procedure to circuits with multiple ( $>3$ ) ports is trivial.

From the perspective of the MOT-PWTD solver, lumped circuits are modeled as impressed voltages at the corresponding circuit loading points in  $S \cup V$ . An arbitrary two-port circuit is depicted in Fig. 1(a). This two-port is assumed to be embedded in a node of a discretized wire or on the edge of a surface triangle. Therefore, the total current that flows in and out of the circuit at a given time step is described by one unknown current coefficient in the MOT-PWTD solver. The presence of  $n_{lc}^{2\text{-port}}$  such two-port circuits is taken into account in the MOT-PWTD system of equations by introducing, on the LHS of (5), an additional time-dependent vector  $\mathcal{V}_j^{lc,2\text{-port}}$  whose elements are given by

$$\mathcal{V}_{j,m}^{lc,2\text{-port}} = \begin{cases} \left[ \partial_t V_j^{lc,i}(g_k^s(t)) \right]_{t=t_j}, & \text{if } m = k \\ 0, & \text{if } m \neq k \end{cases} \quad (14)$$

where  $V_j^{lc,i}$  is the instantaneous voltage at time  $t_j$  of the  $i$ th two-port circuit ( $i = 1, \dots, n_{lc}^{2\text{-port}}$ ), which depends on the loading-point current  $g_k^s(t)$ .

The treatment of two-port lumped circuits can be extended to include three-port lumped circuits. An arbitrary three-port circuit along with the requisite current and voltage conventions is pictured in Fig. 1(b). Three-port circuits reside in junctions between three wire ends or surface edges. Currents through such junctions are described by two spatial basis functions. Since  $I_{1,j}^{lc} + I_{2,j}^{lc} + I_{3,j}^{lc} = 0$ , the two spatial basis functions associated with the three-port lumped circuit are defined to satisfy  $I_{1,j}^{lc} = I_{k,j}^{s,w}$ ,  $I_{2,j}^{lc} = -I_{k,j}^{s,w} - I_{1,j}^{s,w}$ , and  $I_{3,j}^{lc} = I_{l,j}^{s,w}$  [Fig. 1(c)].

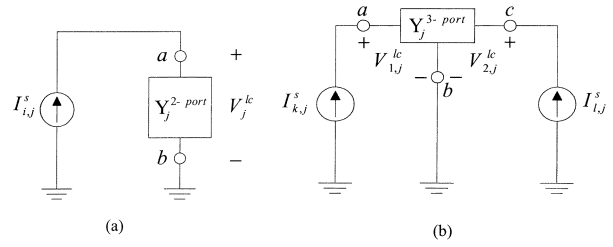


Fig. 2. (a) Two-port circuit with a designated reference node. (b) Three-port circuit with terminal voltages definitions.

Accordingly, two impressed voltages  $V_{l,j}^{lc}$  and  $V_{2,j}^{lc}$  are incorporated into the MOT-PWTD formalism as

$$\mathcal{V}_{j,m}^{lc,3\text{-port}} = \begin{cases} \left[ \partial_t V_{1,j}^{lc,i}(g_k^s(t), g_l^s(t)) \right]_{t=t_j}, & \text{if } m = k \\ \left[ \partial_t V_{2,j}^{lc,i}(g_k^s(t), g_l^s(t)) \right]_{t=t_j}, & \text{if } m = l \\ 0, & \text{else} \end{cases} \quad (15)$$

for  $i = 1, \dots, n_{lc}^{3\text{-port}}$ . After accounting for all two-port and three-port lumped circuits, (5) can be recast as

$$\mathcal{Z}_0 \mathcal{I}_j + \mathcal{V}_j^{lc,2\text{-port}} + \mathcal{V}_j^{lc,3\text{-port}} = \mathcal{F}_j - \sum_{i=1}^{j-1} \mathcal{Z}_i \mathcal{I}_{j-i}. \quad (16)$$

From the perspective of the MNA formalism, the coupled basis function currents can be treated as independent current sources. In each case, the circuit equations can be written as

$$\mathcal{I}_j^{\text{coup}} + \mathcal{Y} \mathcal{V}_j + \mathcal{Y}_j^{nl}(\mathcal{V}_j) = \mathcal{J}_j + \mathcal{J}_j^{nl}(\mathcal{V}_j) \quad (17)$$

where  $\mathcal{I}_j^{\text{coup}}$  contains the contributions of the loading point current coefficients  $I_{k,j}^s$ . Then, for a two-port lumped circuit [see Fig. 2(a)], we have

$$\mathcal{I}_{j,m}^{\text{coup}} = \begin{cases} -I_{k,j}^s, & m = \text{node } a \\ 0, & m \neq \text{node } a. \end{cases} \quad (18)$$

For a three-port lumped circuit, the coupled basis function currents are assumed to flow into the device as shown in Fig. 2(b). In this case,

$$\mathcal{I}_{j,m}^{\text{coup}} = \begin{cases} -I_{k,j}^s, & m = \text{node } a \\ -I_{l,j}^s, & m = \text{node } c \\ 0, & \text{else.} \end{cases} \quad (19)$$

The above procedure can be extended trivially to circuits with multiple ( $>3$ ) ports. Combining (16) and (17) yields the following hybrid field-circuit system of equations at time  $t_j$ :

$$\begin{bmatrix} \mathcal{Z}_0 & \mathcal{C}^v \\ \mathcal{C}^i & \mathcal{Y} \end{bmatrix} \begin{bmatrix} \mathcal{I}_j \\ \mathcal{V}_j \end{bmatrix} + \begin{bmatrix} \mathbf{0} \\ \mathcal{Y}_j^{nl}(\mathcal{V}_j) \end{bmatrix} = \begin{bmatrix} \mathcal{F}_j - \sum_{i=1}^{j-1} \mathcal{Z}_i \mathcal{I}_{j-i} - \mathcal{K}_j^v \\ \mathcal{J}_j \end{bmatrix} + \begin{bmatrix} \mathbf{0} \\ \mathcal{J}_j^{nl}(\mathcal{V}_j) \end{bmatrix}. \quad (20)$$

Here,  $\mathcal{C}^i$  contains the information from  $\mathcal{I}^{\text{coup}}$  for each two-port and three-port lumped circuit and consists of only  $-1$ 's,  $0$ 's, and  $+1$ 's. The lumped circuit voltage contributions are contained in both  $\mathcal{C}^v$  and  $\mathcal{K}_j^v$ . In practice, temporal derivatives are evaluated using a third-order backward differentiation rule

$$\partial_t V_j = \frac{1}{2\Delta t} \left( \frac{11}{3} V_j - 6V_{j-1} + 3V_{j-2} - \frac{2}{3} V_{j-3} \right). \quad (21)$$

The matrix  $C^v$  contains the coefficient of the first term in (21), and the remaining terms are used to evaluate the vector  $\mathcal{K}_j^v$ . Thus, it is necessary to store the pertinent lumped circuit voltages from the previous three time steps for each lumped circuit.

The solution of (20) proceeds as follows. If the lumped circuits are linear (note that linear inductors and capacitors are included in this context), the overall system of equations is solved at each time step iteratively using an iterative scheme, e.g., TFQMR. If nonlinear circuit elements are included in the network, a different iterative scheme is used employing both Newton's method and the TFQMR. Let  $\mathcal{V}_j = [\mathcal{V}_j^l \mathcal{V}_j^{nl}]^T$ , where  $\mathcal{V}_j^l$  and  $\mathcal{V}_j^{nl}$  denote the node voltages at time  $t_j$  that have linear and nonlinear dependencies, respectively. Also, by definition,  $\mathcal{Y}_j^{nl}(\mathcal{V}_j) = \mathcal{Y}_j^{nl}([0 \mathcal{V}_j^{nl}]^T)$  and  $\mathcal{J}_j^{nl}(\mathcal{V}_j) = \mathcal{J}_j^{nl}([0 \mathcal{V}_j^{nl}]^T)$ . The solver at the  $k$ th iteration then proceeds as follows.

- 1) Evaluate  $\mathcal{Y}_j^{nl}(\mathcal{V}_j^k)$  and  $\mathcal{J}_j^{nl}(\mathcal{V}_j^k)$ , where  $\mathcal{V}_j^k = [0 \mathcal{V}_j^{nl,k}]^T$  and  $\mathcal{V}_j^{nl,k}$  is the guess provided by the nonlinear solver in the  $k$ th iteration.
- 2) Solve the resulting "linearized" system of equations

$$\begin{bmatrix} \mathcal{Z}_0 & C^v \\ C^i & \mathcal{Y} \end{bmatrix} \begin{bmatrix} \tilde{\mathcal{I}}_j^k \\ \tilde{\mathcal{V}}_j^k \end{bmatrix} = \begin{bmatrix} \mathcal{F}_j - \sum_{i=1}^{j-1} \mathcal{Z}_i \mathcal{I}_{j-i} - \mathcal{K}_j^v \\ \mathcal{J}_j - \mathcal{Y}_j^{nl}(\mathcal{V}_j^k) + \mathcal{J}_j^{nl}(\mathcal{V}_j^k) \end{bmatrix} \quad (22)$$

using the iterative solver.

- 3) Extract  $\tilde{\mathcal{V}}_j^{nl,k}$  from  $\tilde{\mathcal{V}}_j^k = [\tilde{\mathcal{V}}_j^l \tilde{\mathcal{V}}_j^{nl,k}]^T$ .
- 4) Check if  $\mathcal{V}_j^{nl,k} - \tilde{\mathcal{V}}_j^{nl,k} = \mathbf{0}$ . If not, evaluate  $\mathcal{V}_j^{nl,k+1}$  via Newton's update algorithm.

Repeating the above iterative procedure until convergence gives the solution for  $[\mathcal{I}_j \mathcal{V}_j]^T$  in (20). After the solution has been determined, the equivalent sources for all inductors and capacitors are updated.

Two important observations are in place here. First, note that the time step size in the simulation is assumed to be constant and is dictated by the MOT-PWTD algorithm. Hence, it is usually chosen to be sufficiently small so that the initial guess to the nonlinear system of equations, which is the solution from the previous time step, is close enough to the actual solution and the number of Newton iterations remains small. Second, for most problems of interest in this study, the number of electromagnetic equations dominates the number of circuit equations, i.e.,  $N_{sv} \gg N_c$ . It can be argued then, as a consequence of these two observations, that the majority of the computational cost in solving (20) remains in the construction of the RHS of the MOT system. As discussed in Section II-A, this cost can be drastically reduced using the multilevel PWTD algorithm, which enables the fast and accurate simulation of complex structures loaded with linear/nonlinear lumped circuits.

### III. ANALYSIS OF A NONLINEAR ACTIVE MICROWAVE AMPLIFIER

The microwave amplifier shown in Fig. 3(a) has been previously analyzed using the FDTD and FETD methods in [9] and [13], and [14], respectively. Here, the same amplifier is analyzed using the hybrid field-circuit simulator described in the previous section. The problem geometry is modeled using

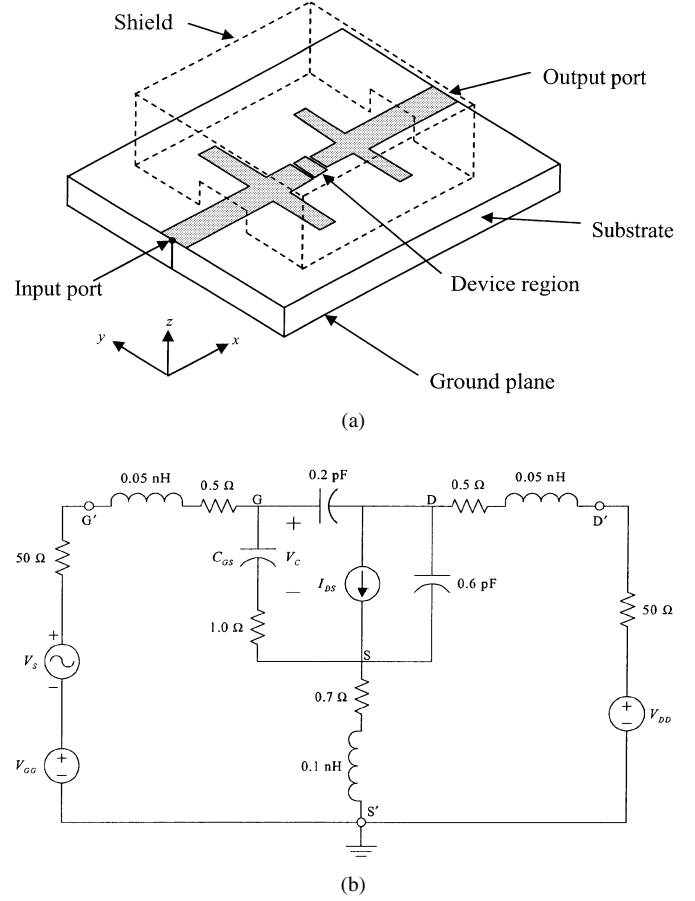


Fig. 3. (a) Microwave amplifier with shielding structure. (b) Circuit model of the MEFET.

PEC microstrip lines that reside on a finite dielectric substrate ( $\epsilon_r = 2.33$ ) backed by a conforming finite PEC ground plane. All dimensions pertinent to the geometrical definition of the structure (except for the size of the ground plane) are given in [9] and are not repeated here. The lumped circuits in the problem comprise of a nonlinear MEFET that resides at the center of the structure and the linear termination networks at the input and output ports [see Fig. 3(a)]. The large-signal circuit model for the MEFET is shown in Fig. 3(b). The equations that describe the behavior of the nonlinear current source  $I_{DS}$  and the nonlinear capacitor  $C_{GS}$  are identical to those used in [9]. Note that this particular circuit representation is based on the Curtice–Cubic model [38]. Although the model presented in [38] is slightly more complex than the one described in [9], here the model from [9] has been utilized without any modifications to allow for a consistent comparison of results. The input and output ports are both terminated with lumped 50- $\Omega$  resistors.

In what follows, first, the amplifier is simulated without the shield and the calculated  $S$ -parameters are compared to those obtained using HP ADS [39]. Next, the shield is included in the simulation, and for a number of different shielding geometries, the change on the  $S$ -parameters is examined. Finally, the shielding effectiveness of the structure to EMI due to various external excitations is investigated by observing transient waveforms at various ports in the system.

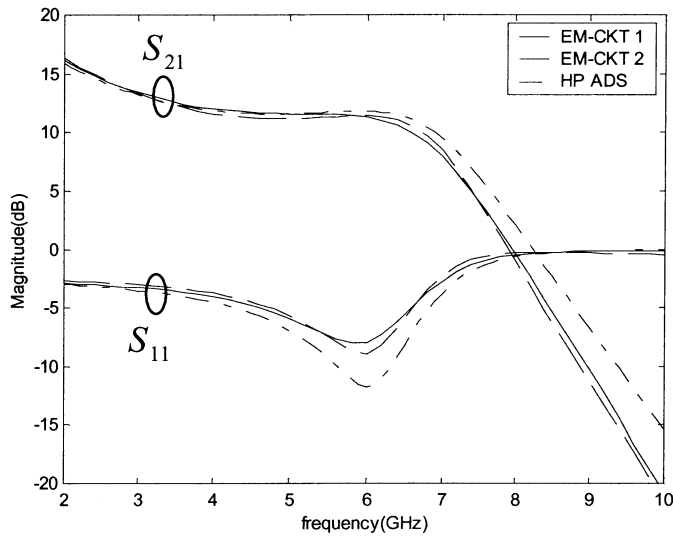


Fig. 4.  $S_{11}$  and  $S_{21}$  of the amplifier without a shield.

#### A. Calculation of the $S$ -Parameters

To calculate the  $S$ -parameters of the microwave amplifier without the shielding structure, two different spatial meshes corresponding to ground plane sizes of  $690 \times 640 \text{ mm}^2$  and  $960 \times 650 \text{ mm}^2$ , are constructed. Both meshes support frequencies up to 10 GHz. The resulting number of electromagnetic unknowns is  $N_{sv} = 5269$  and  $N_{sv} = 8564$ , respectively. The voltage at the input port is supplied by a delta-gap source with a modulated Gaussian temporal signature

$$V_S(t) = \cos [2\pi f_0 (t - t_p)] \exp \left[ -\frac{(t - t_p)^2}{2\sigma^2} \right] \quad (23)$$

where  $f_0 = 6 \text{ GHz}$ ,  $\sigma = 3/14\pi \text{ ns}$ , and  $t_p = 6\sigma \text{ s}$ . The amplitude of the input pulse is chosen sufficiently small such that the MESFET operates in the linear regime. In all simulations presented herein, the time step size is 5 ps. The dc operating point of the MESFET is chosen as  $V_{G'S'} = -0.81 \text{ V}$  and  $V_{D'S'} = 6.4 \text{ V}$  [9].

The  $S$ -parameters calculated at the source and load points by the hybrid field-circuit simulator are compared with HP ADS results in Fig. 4. The agreement between the two sets of data is satisfactory. The largest discrepancy is in the  $S_{21}$  data at frequencies above 7 GHz, which could be due to a number of factors, including the particular  $S$ -parameter extraction method utilized. A more accurate way to determine  $S$ -parameters is to calculate the incident and reflected waves on the input and output microstrip line sections using de-embedding techniques, for example, the one described in [40]. It is interesting to note, however, that the size of the finite ground plane has little to no effect on the  $S$ -parameters for the two cases considered here (in Fig. 4, EM-CKT1 and EM-CKT 2 correspond to ground planes of size  $960 \times 650 \text{ mm}^2$  and  $690 \times 640 \text{ mm}^2$ , respectively).

TABLE I  
DIMENSIONS FOR DIFFERENT TEST CASES FOR THE SHIELDED AMPLIFIER

Case Name	Size of ground plane (mil <sup>2</sup> )	Dimensions of shield (mil <sup>2</sup> )	Size of holes (mil <sup>2</sup> )
EM-CKT-1	960×650	960×650×186	365×93
EM-CKT-2	690×640	690×640×186	365×93
EM-CKT-3	690×640	690×640×186	200×48
EM-CKT-4	690×640	no shield	-

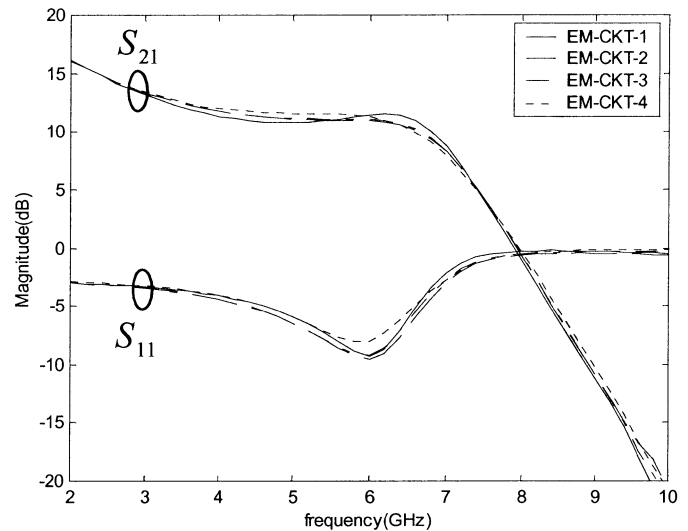


Fig. 5.  $S_{11}$  and  $S_{21}$  of an amplifier with and without a shield.

#### B. Amplifier With a Shielding Structure

Next, the shield is included in the simulation and again the  $S$ -parameters are calculated. The shield in [9] is composed of PEC material and has dimensions of  $690 \times 640 \times 186 \text{ mm}^3$ . The dimensions of the two rectangular holes near the input and output microstrip lines, however, are not given in [9]. Here, a number of different configurations that correspond to different ground plane, shield, and hole dimensions are considered. All cases are summarized in Table I and the  $S$ -parameters calculated for each case are plotted in Fig. 5. The results indicate that all shielding geometries studied here have a very similar effect on the operation of the amplifier and hence the  $S$ -parameters. Except for an additional dip in  $S_{21}$  around 9 GHz, the trends reported in [9] are also observed here. The frequency of the matching dip in  $S_{11}$  remains unchanged but decreases by approximately 1 dB, while there is a slight increase in the gain around 6.5 GHz, which is more outspoken for the large ground plane than for the small one.

#### C. Shielding Performance of the Complete Structure

Here, the amplifier is excited by both the delta-gap voltage source defined by (23) and a variety of plane-wave pulses that represent EMI due to an external source. The objective is to compare the time-domain responses at the input and output ports of the transistor when the additional plane-wave pulse is incident upon the amplifier with and without the shield. This way, the amount of energy coupled to the transistor, either directly,

through the input and output microstrip sections (which remain partially exposed to the plane-wave signal when the shield is present), and through the shield holes when the shield is present, can be observed. In the following examples, the simulated geometry has the dimensions labeled EM-CKT-1 in Table I and the plane-wave excitation is a modulated Gaussian pulse defined by

$$\mathbf{E}^i(\mathbf{r}, t) = \mathbf{E}_0 \cos \left[ 2\pi f_0 \left( t - t_p - \frac{\hat{\mathbf{k}} \cdot \mathbf{r}}{c} \right) \right] \times \exp \left[ -\frac{\left( t - t_p - \frac{\hat{\mathbf{k}} \cdot \mathbf{r}}{c} \right)^2}{2\sigma^2} \right] \quad (24)$$

where

$$\begin{aligned} \mathbf{E}_0 &= E_x \hat{\mathbf{x}} + E_y \hat{\mathbf{y}} + E_z \hat{\mathbf{z}} \\ \hat{\mathbf{k}} &= k_x \hat{\mathbf{x}} + k_y \hat{\mathbf{y}} + k_z \hat{\mathbf{z}}. \end{aligned} \quad (25)$$

Given the parameters  $E_0$ ,  $E_\phi$ ,  $\theta_i$ , and  $\phi_i$ , the quantities in (24) are calculated using

$$\begin{aligned} E_x &= E_\theta \cos \theta_i \cos \phi_i - E_\phi \sin \phi_i \\ k_x &= \sin \theta_i \cos \phi_i \\ E_y &= E_\theta \cos \theta_i \sin \phi_i + E_\phi \cos \phi_i \\ k_y &= \sin \theta_i \sin \phi_i \\ E_z &= -E_\theta \sin \theta_i \\ k_z &= \cos \theta_i. \end{aligned} \quad (26)$$

In the first example, the plane-wave excitation has the parameters

$$\begin{aligned} f_0 &= 4 \text{ GHz} \\ \sigma &= \frac{1}{4\pi} \text{ ns} \\ E_\theta &= -500 \text{ V/m} \\ \theta_i &= 145^\circ \\ t_p &= 0.5 \text{ ns} \\ E_\phi &= -500 \text{ V/m} \\ \phi_i &= 0^\circ \end{aligned} \quad (27)$$

and represents a pulse traveling in the  $\hat{\mathbf{k}} = 0.5736\hat{\mathbf{x}} - 0.8192\hat{\mathbf{z}}$  direction toward the input section of the amplifier. Both the center frequency and bandwidth of the plane-wave signature differ from that of the delta-gap source. Fig. 6(a) shows the input ac voltage to the lumped transistor with only the delta-gap voltage source active and no shield present, with both the delta-gap and plane-wave sources active and no shield present, and with both the delta-gap and plane-wave sources active and the shield present. Fig. 6(b) is a similar plot showing the output voltage of the lumped transistor under the same three conditions. As is evident from the early-time responses, some of the energy from the plane wave is indeed coupled to the transistor from the input microstrip line, though for this particular plane-wave excitation, the shield effectively prevents most of the interference.

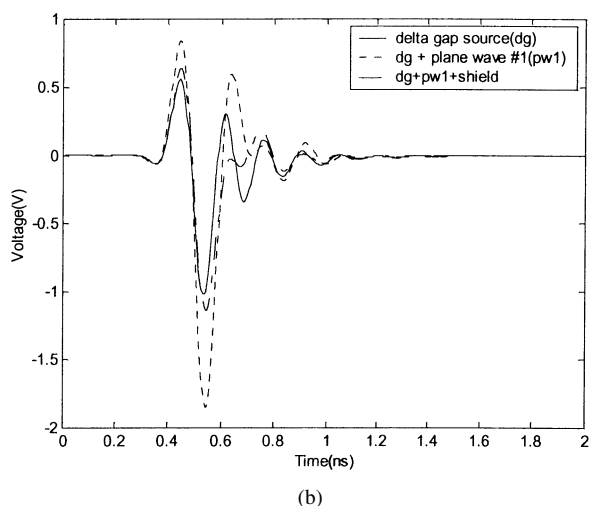
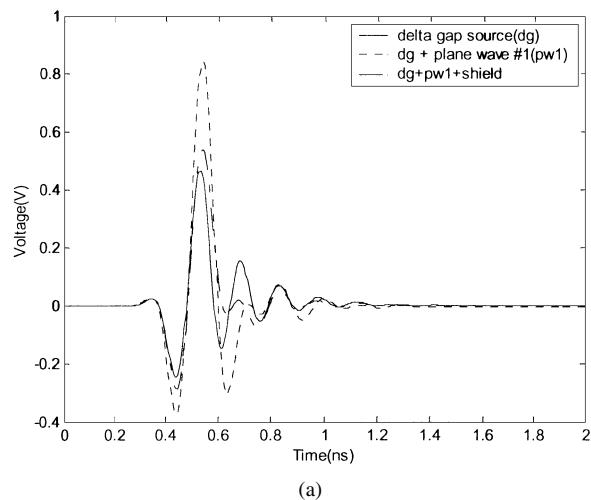


Fig. 6. Time-domain response at: (a) input and (b) output of transistor for  $\theta_i = 145^\circ$ ,  $\phi_i = 0^\circ$ .

In the second example, the plane wave has the parameters

$$\begin{aligned} f_0 &= 3 \text{ GHz} \\ \sigma &= \frac{3}{14\pi} \text{ ns} \\ E_\theta &= -500 \text{ V/m} \\ \theta_i &= 115^\circ \\ t_p &= 0.5 \text{ ns} \\ E_\phi &= +500 \text{ V/m} \\ \phi_i &= 45^\circ \end{aligned} \quad (28)$$

and represents a pulse traveling in the  $\hat{\mathbf{k}} = 0.6409(\hat{\mathbf{x}} + \hat{\mathbf{y}}) - 0.4226\hat{\mathbf{z}}$  direction, toward the input section of the amplifier, but from a  $45^\circ$  angle. While both signals have identical bandwidths, the center frequency of the plane-wave signal is lower than the operating frequency of the amplifier. The input and output voltage of the lumped transistor are shown in Fig. 7(a) and (b), respectively, under the same three conditions as before. In this example, the plane wave has much less of an effect on the amplifier without the shield. Hence, in this case, we observe “shield-induced” interference more in the transient waveforms.

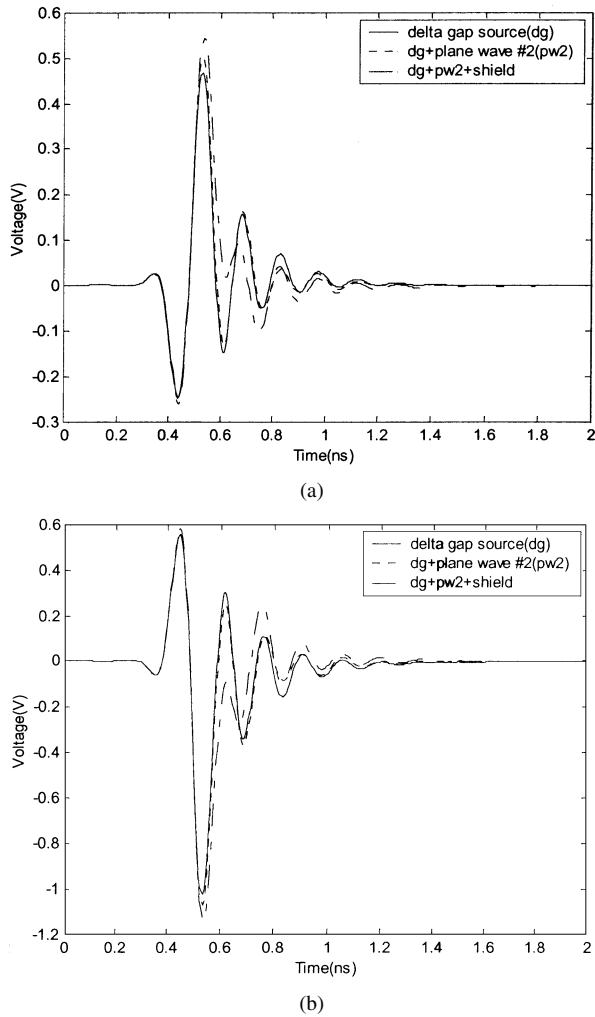


Fig. 7. Time-domain response at: (a) input and (b) output of transistor for  $\theta_i = 115^\circ$  and  $\phi_i = 45^\circ$ .

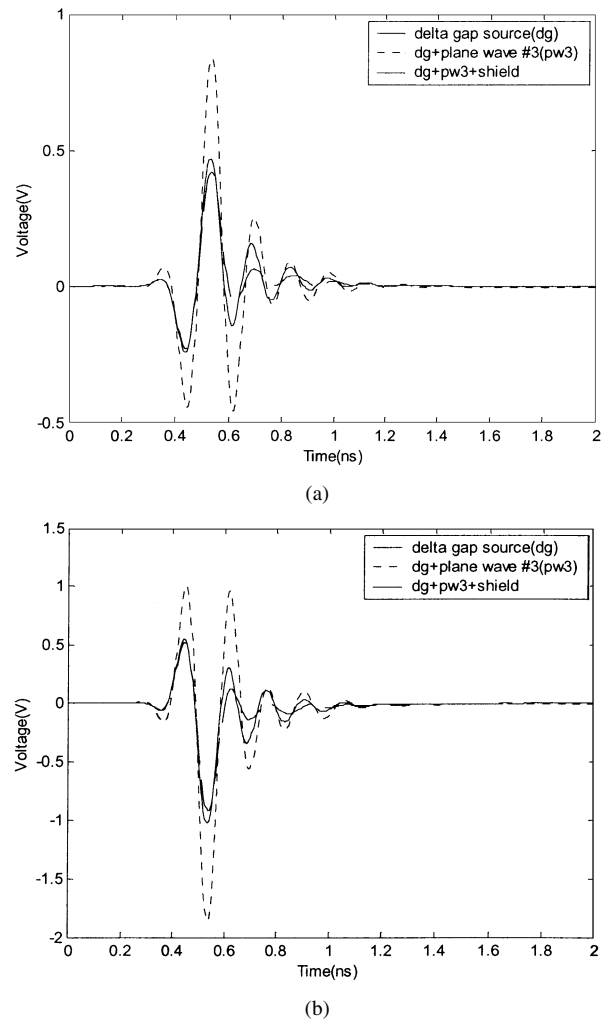


Fig. 8. Time-domain response at: (a) input and (b) output of the transistor for  $\theta_i = 180^\circ$  and  $\phi_i = 0^\circ$ .

In the third example, the plane wave has the parameters

$$\begin{aligned}
 f_0 &= 6 \text{ GHz} \\
 \sigma &= \frac{3}{11\pi} \text{ ns} \\
 E_\theta &= -500 \text{ V/m} \\
 \theta_i &= 180^\circ \\
 t_p &= 0.5 \text{ ns} \\
 E_\phi &= +500 \text{ V/m} \\
 \phi_i &= 0^\circ
 \end{aligned} \tag{29}$$

and represents a pulse traveling in the  $\hat{\mathbf{k}} = -\hat{\mathbf{z}}$  direction, from above and normal to the microstrip lines. The center frequency of the plane-wave signal coincides with the operating frequency of the amplifier. The voltages at the input and output of the transistor are shown in Fig. 8(a) and (b). For this normally incident pulse, we observe the largest amount of EMI on the operation of the amplifier without the shield. However, the shield also acts very efficiently in this case as it prevents any direct exposure of the microstrips to the incident plane wave.

In the final example, the amplifier is placed at the center of a larger PEC enclosure that contains three equally sized holes on

one side of the enclosure. The dimensions of the PEC enclosure are shown in Fig. 9. The incident plane wave has the parameters

$$\begin{aligned}
 f_0 &= 4 \text{ GHz} \\
 \sigma &= \frac{1}{4\pi} \text{ ns} \\
 E_\theta &= +500 \text{ V/m} \\
 \theta_i &= 135^\circ \\
 t_p &= 0.5 \text{ ns} \\
 E_\phi &= +500 \text{ V/m} \\
 \phi_i &= 180^\circ.
 \end{aligned} \tag{30}$$

The overall geometry has been discretized using  $N_{sv} = 17927$  basis functions. The voltages at the input and output of the transistors in this case are shown in Fig. 10(a) and (b), respectively.

The above examples illustrate a simple scenario where the EMI from external sources is modeled using a plane-wave excitation model. It is also assumed here that the aforementioned large-signal model for the MESFET remains valid for all of the above excitations. A careful examination of the magnitude of the voltages at the input and output ports of the transistor and

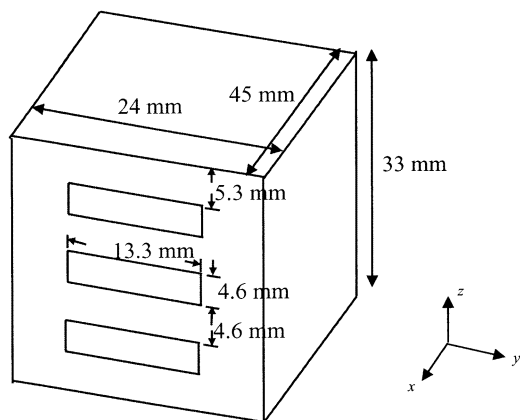
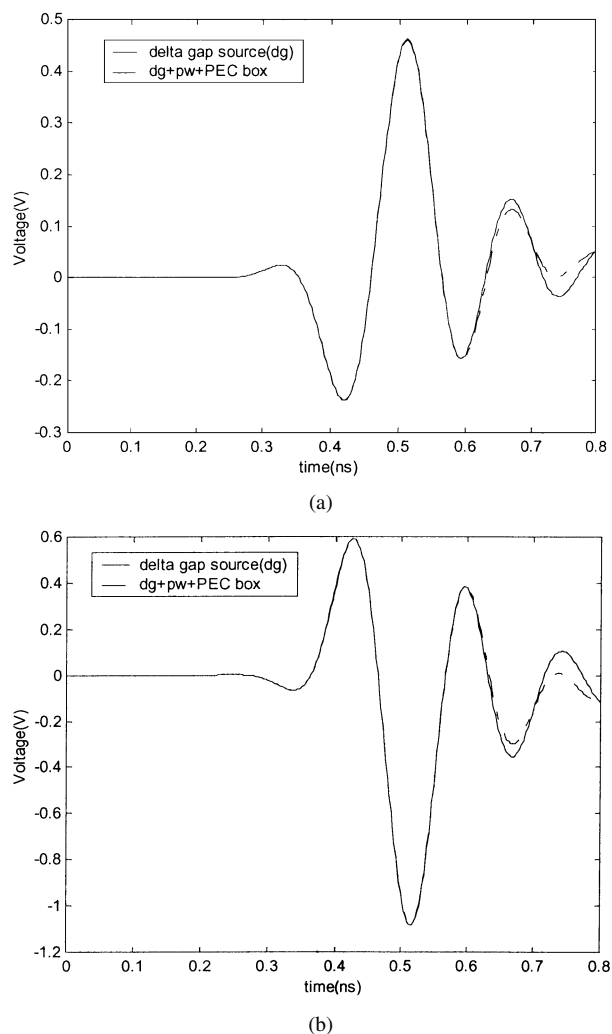


Fig. 9. Dimensions of the larger PEC enclosure.


 Fig. 10. Time-domain response at: (a) input and (b) output of the transistor for  $\theta_i = 135^\circ$  and  $\phi_i = 180^\circ$ .

comparison of the MESFET model of [9] to that of the original Curtice–Cubic model in [38] has revealed that this assumption is indeed true for all the cases considered here. In most real-life scenarios, the EMI source can be a lot more difficult to identify and more complete device models may need to be incorporated into the solution scheme. Nonetheless, the results presented here

still demonstrate the capability of the proposed hybrid field-circuit simulator to analyze such problems in an efficient and accurate way.

The reduced computational complexity of PWTD-accelerated MOT-based field solvers has been demonstrated previously in the literature by experimentally verifying the asymptotical scaling laws for these algorithm [28], [31]. Here, we concentrate on simulation of a specific geometry (i.e., the geometry labeled EM-CKT-4 in Table I) to assess the computational efficiency of the proposed hybrid field-circuit solver. The number of electromagnetic and circuit unknowns for this geometry are  $N_{sv} = 5269$  and  $N_c = 12$ , respectively. There are two nonlinear circuit elements [i.e., the nonlinear current source and the nonlinear capacitor in Fig. 3(b)]. Analysis of this geometry for 500 time steps using a time step size of 5 ps requires 35 min of CPU time on a 2.4-GHz Pentium IV PC operating on the Linux platform. Note that all the other simulations performed in this study to generate the results presented require very similar computational resources.

#### IV. CONCLUSION

In this paper, arbitrary linear and nonlinear lumped circuits are included in a fast MOT-PWTD algorithm by introducing a MNA-based SPICE-like transient circuit simulator to construct and evaluate the circuit equations in a manner consistent with the TDIE framework. In the proposed methodology, the systems of equations for both the TDIE and MNA are coupled together, allowing the complete system of equations to be solved simultaneously. The resulting algorithm is applied to analysis of a shielded microwave amplifier. Overall, the hybrid field-circuit simulator proposed here lends itself to applications where arbitrarily complex lumped circuits are considered, for which the derivation of the time-domain circuit equations is cumbersome. As the development of fast TDIE solvers continues, the ability for handling lumped circuits is expected to play a significant role in the applicability to larger and more complex systems.

Most modern time-domain circuit simulators incorporate dynamic time-step control algorithms to improve speed and accuracy. Thus, one further extension to this work would be to develop a method in which the field solver and transient circuit simulator could function together, but with variable time-step sizes dictated by the circuit equations. Along the same line, more complex nonlinear transistor models could be incorporated into the transient circuit simulator, in an effort to further narrow the gap between the simulator developed here and commercial simulators such as SPICE.

#### REFERENCES

- [1] W. Sui, D. A. Christensen, and C. H. Durney, "Extending the two-dimensional FDTD method to hybrid electromagnetic systems with active and passive lumped elements," *IEEE Trans. Microwave Theory Tech.*, vol. 40, pp. 724–730, Apr. 1992.
- [2] M. Picket-May, A. Taflove, and J. Baron, "FD-TD modeling of digital signal propagation in 3-D circuits with passive and active loads," *IEEE Trans. Microwave Theory Tech.*, vol. 42, pp. 1514–1523, Aug. 1994.
- [3] P. Ciampolini, P. Mezzanotte, L. Roselli, and R. Sorrentino, "Accurate and efficient circuit simulation with lumped-element FDTD technique," *IEEE Trans. Microwave Theory Tech.*, vol. 44, pp. 2207–2215, Dec. 1996.

- [4] V. A. Thomas, M. E. Jones, M. Piket-May, A. Taflove, and E. Harrigan, "The use of SPICE lumped circuits as sub-grid models for FDTD analysis," *IEEE Microwave Guided Wave Lett.*, vol. 4, pp. 141–143, May 1994.
- [5] C. Kuo, V. A. Thomas, S. T. Chew, B. Houshmand, and T. Itoh, "Small signal analysis of active circuits using FDTD algorithm," *IEEE Microwave Guided Wave Lett.*, vol. 5, pp. 216–218, July 1995.
- [6] A. Witzig, C. Schuster, P. Regli, and W. Fichtner, "Global modeling of microwave applications by combining the FDTD method and a general semiconductor device and circuit simulator," *IEEE Trans. Microwave Theory Tech.*, vol. 47, pp. 919–928, June 1999.
- [7] Y. Tsuei, A. C. Cangellaris, and J. L. Prince, "Rigorous electromagnetic modeling of chip-to-package (first-level) interconnections," *IEEE Trans. Comp., Hybrids, Manufact. Technol.*, vol. 16, pp. 876–883, Dec. 1993.
- [8] N. Orhanovic, R. Raghuram, and N. Matsui, "Full wave analysis of planar interconnect structures using FDTD-SPICE," in *Proc. Electronic Components and Technology Conf.*, 2001, pp. 489–494.
- [9] C. Kuo, B. Houshmand, and T. Itoh, "Full-wave analysis of packaged microwave circuits with active and nonlinear devices: An FDTD approach," *IEEE Trans. Microwave Theory Tech.*, vol. 45, pp. 819–826, May 1997.
- [10] V. S. Reddy and R. Garg, "An improved extended FDTD formulation for active microwave circuits," *IEEE Trans. Microwave Theory Tech.*, vol. 47, pp. 1603–1608, Sept. 1999.
- [11] P. Russer, P. P. M. So, and W. J. R. Hoefer, "Modeling of nonlinear active regions in TLM," *IEEE Microwave Guided Wave Lett.*, vol. 1, pp. 10–13, Jan. 1991.
- [12] K. Guillouard, M. F. Wong, V. F. Hanna, and J. Citerne, "A new global time-domain electromagnetic simulator of microwave circuits including lumped elements based on finite-element method," *IEEE Trans. Microwave Theory Tech.*, vol. 47, pp. 2045–2049, Oct. 1999.
- [13] S. Chang, R. Coccioli, Y. Qian, and T. Itoh, "A global finite-element time-domain analysis of active nonlinear microwave circuits," *IEEE Trans. Microwave Theory Tech.*, vol. 47, pp. 2410–2416, Dec. 1999.
- [14] H.-P. Tsai, Y. Wang, and T. Itoh, "An unconditionally stable extended (USE) finite-element time-domain solution of active nonlinear microwave circuits using perfectly matched layers," *IEEE Trans. Microwave Theory Tech.*, vol. 50, pp. 2226–2232, Oct. 2002.
- [15] S. R. Cloude, I. Frost, P. D. Smith, and A. Milne, "Time domain integral equation methods for nonlinear systems," in *Proc. IEE Int. Conf. Computation in Electromagnetics*, Nov. 1991, pp. 300–303.
- [16] A. Orlandi, "Lightning induced transient voltages in presence of complex structures and nonlinear loads," *IEEE Trans. Electromagn. Compat.*, vol. 38, pp. 150–155, May 1996.
- [17] M. F. Pantoja, A. R. Bretones, and R. G. Martin, "Time-domain analysis of thin-wire loaded antennas using integral equations," *Proc. Inst. Elect. Eng.*, pt. H, vol. 147, pp. 203–206, June 2000.
- [18] A. E. Ruehli, "Equivalent circuit models for three dimensional multiconductor systems," *IEEE Trans. Microwave Theory Tech.*, vol. MTT-22, pp. 216–221, Mar. 1974.
- [19] W. Pinello, A. C. Cangellaris, and A. Ruehli, "Hybrid electromagnetic modeling of noise interactions in packaged electronics based on the partial-element equivalent-circuit formulation," *IEEE Trans. Microwave Theory Tech.*, vol. 45, pp. 1889–1896, Oct. 1997.
- [20] P. J. Restle, A. E. Ruehli, S. G. Walker, and G. Papadopoulos, "Full-wave PEEC timedomain method for the modeling of on-chip interconnects," *IEEE Trans. Computer-Aided Design*, vol. 20, pp. 877–897, July 2001.
- [21] V. Jandhyala, Y. Wang, D. Gope, and C. J. R. Shi, "A surface-based integral-equation formulation for coupled electromagnetic and circuit simulation," *Microwave Opt. Technol. Lett.*, vol. 34, pp. 103–106, July 2002.
- [22] C. Yang and V. Jandhyala, "A time domain surface integral technique for mixed electromagnetic and circuit simulation," Univ. Washington, Seattle, WA, UWEE Tech. Rep. UWEETR-2003-0001, 2003.
- [23] J. Garrett, A. E. Ruehli, and C. R. Paul, "Accuracy and stability improvements of integral equation models using the partial element equivalent circuit (PEEC) approach," *IEEE Trans. Antennas Propagat.*, vol. 46, pp. 1824–1832, Dec. 1998.
- [24] S. M. Rao and T. K. Sarkar, "Transient analysis of electromagnetic scattering from wire structures utilizing an implicit time-domain integral-equation technique," *Microwave Opt. Technol. Lett.*, vol. 17, pp. 66–69, Jan. 1998.
- [25] M. J. Bluck and S. P. Walker, "Time-domain BIE analysis of large three-dimensional electromagnetic scattering problems," *IEEE Trans. Antennas Propagat.*, vol. 45, pp. 894–901, May 1997.
- [26] A. A. Ergin, B. Shanker, and E. Michielssen, "The plane wave time domain algorithm for the fast analysis of transient wave phenomena," *IEEE Antennas Propagat. Mag.*, vol. 41, pp. 39–52, Aug. 1999.
- [27] ———, "Fast evaluation of three-dimensional transient wave fields using diagonal translation operators," *J. Comput. Phys.*, vol. 146, pp. 157–180, Oct. 1998.
- [28] K. Aygün, B. Shanker, A. A. Ergin, and E. Michielssen, "A two-level plane wave time domain algorithm for fast analysis of EMC/EMI problems," *IEEE Trans. Electromagn. Compat.*, vol. 44, pp. 152–164, Feb. 2002.
- [29] K. Aygün, B. Shanker, and E. Michielssen, "Fast time-domain characterization of finite size microstrip structures," *Int. J. Numer. Modeling*, vol. 15, no. 5-6, pp. 439–457, 2002.
- [30] K. Aygün, S. E. Fisher, A. A. Ergin, B. Shanker, and E. Michielssen, "Transient analysis of multielement wire antennas mounted on arbitrarily shaped perfectly conducting bodies," *Radio Sci.*, vol. 34, pp. 781–796, 1999.
- [31] B. Shanker, A. A. Ergin, and E. Michielssen, "Fast analysis of electromagnetic scattering phenomena using the multilevel plane wave time domain algorithm," Univ. Illinois at Urbana-Champaign, Urbana, IL, CCEM Rep. 10-01, 2001.
- [32] L. W. Nagel, "SPICE2: A computer program to simulate semiconductor circuits," Univ. California, Berkeley, CA, Memo UCB/ERL M75/520, 1975.
- [33] A. Vladimirescu, *The SPICE Book*. New York: Wiley, 1994.
- [34] C. Ho, A. E. Ruehli, and P. A. Brennan, "The modified nodal approach to network analysis," *IEEE Trans. Circuits Syst.*, vol. CAS-22, pp. 504–509, June 1975.
- [35] Y. Saad, *Iterative Methods for Sparse Linear Systems*. New York: PWS, 1996.
- [36] W. H. Press, S. A. Teukolsky, W. T. Vetterling, and B. P. Flannery, *Numerical Recipes in Fortran*. New York: Cambridge Univ. Press, 1992.
- [37] B. C. Fischer, "Incorporation of arbitrary linear and nonlinear lumped circuits into a fast time-domain integral equation solver," M.S. thesis, Dept. Elect. Comput. Eng., Univ. Illinois at Urbana-Champaign, Urbana, IL, 2002.
- [38] W. R. Curtice, "GaAs MESFET modeling and nonlinear CAD," *IEEE Trans. Microwave Theory Tech.*, vol. 36, pp. 220–230, Feb. 1988.
- [39] HP-ADS of Hewlett-Packard. [Online]. Available: <http://eesof.tm.agilent.com/products/>
- [40] E. Suter, M. B. Cuadra, and J. R. Mosig, "A comparative study of the input parameter de-embedding techniques for integral equation methods," in *Proc. Eur. Congr. Computational Methods in Applied Sciences and Engineering*, 2000, pp. 1–14.



**Kemal Aygün** received the B.S. degree from the Middle East Technical University, Ankara, Turkey, in 1995, and the M.S. and Ph.D. degrees from the University of Illinois at Urbana-Champaign (UIUC), in 1997 and 2002, respectively.

From 1995 to 2002, he was a Research Assistant with the Center for Computational Electromagnetics, UIUC, where his research was focused on development of novel fast algorithms for transient analysis of antennas and circuits. He is currently with the Intel Corporation, Chandler, AZ.

Dr. Aygün was the recipient of the 1999 and 2000 Computational Science and Engineering Fellowship while at UIUC and the 2002 Yuen T. Lo Award for excellence in research.



**Brian C. Fischer** received the B.S. and M.S. degrees in electrical engineering from the University of Illinois Urbana-Champaign, in 1999 and 2002, respectively.

As a graduate student, he was a Research Assistant with the Center for Computational Electromagnetics, where his primary focus was on time-domain integral equation solvers. He is currently with the Lockheed Martin Corporation, Sunnyvale, CA.

**Jun Meng** received the B.S. and M.S. degrees in electrical engineering from Tsinghua University, Beijing, China, and is currently working toward the Ph.D. degree at the University of Illinois at Urbana-Champaign.

His research interests include fast algorithms for circuit and electromagnetic analysis in the time domain.



**Balasubramaniam Shanker** (M'96–SM'00) received the B.Tech. degree from the Indian Institute of Technology, Madras, India, in 1989, and the M.S. and Ph.D. degrees from the Pennsylvania State University, University Park, in 1992 and 1993, respectively.

From 1993 to 1996, he was a Research Associate with the Department of Biochemistry and Biophysics, Iowa State University, Ames, where he was involved with the molecular theory of optical activity. From 1996 to 1999, he was a Visiting

Assistant Professor with the Center for Computational Electromagnetics, University of Illinois at Urbana-Champaign. From 1999 to 2002, he was an Assistant Professor with the Department of Electrical and Computer Engineering, Iowa State University. He is currently an Associate Professor with the Electrical and Computer Engineering Department, Michigan State University, East Lansing. He has authored/coauthored over 130 papers in archival journals and conference proceedings. His research interests include all aspects of computational electromagnetics, and electromagnetic-wave propagation in complex media.

Dr. Shanker is a full member of the USNC–URSI Commission B.



**Eric Michielssen** (M'95–SM'99–F'02) received the M.S. degree (*summa cum laude*) from the Katholieke Universiteit Leuven (KUL), Leuven, Belgium, in 1987, and the Ph.D. degree from the University of Illinois at Urbana-Champaign (UIUC), in 1992, both in electrical engineering.

He was a Research and Teaching Assistant with the Microwaves and Lasers Laboratory, KUL (1987–1988), and the Electromagnetic Communication Laboratory, UIUC (1988–1992). In 1992, he joined the Faculty of the Department of Electrical and Computer Engineering, UIUC, where he is currently a Professor. Since 1995, he has been Associate Director of the Center for Computational Electromagnetics, UIUC. He has authored or coauthored over 80 journal papers and book chapters and over 100 papers in conference proceedings. His research interests include all aspects of theoretical and applied computational electromagnetics. His principal research focus has been on the development of fast frequency- and time-domain integral-equation-based techniques for analyzing electromagnetic phenomena and the development of robust genetic algorithm-driven optimizers for the synthesis of electromagnetic/optical devices. From 1997 to 1999, he was an Associate Editor for *Radio Science*.

Dr. Michielssen served as the technical chairman of the 1997 Applied Computational Electromagnetics Society (ACES) Symposium (Review of Progress in Applied Computational Electromagnetics, March 1997, Monterey, CA). From 1998 to 2001, he served on the ACES Board of Directors and as ACES vice-president. He is currently an associate editor for the IEEE TRANSACTIONS ON ANTENNAS AND PROPAGATION. He is a Member of URSI Commission B. He was the recipient of a 1988 Belgian American Educational Foundation Fellowship and a 1990 Schlumberger Fellowship. He was also the recipient of a 1994 International Union of Radio Scientists (URSI) Young Scientist Fellowship, a 1995 National Science Foundation CAREER Award, and the 1998 Applied Computational Electromagnetics Society (ACES) Valued Service Award. In addition, he was named 1999 URSI United States National Committee Henry G. Booker Fellow and selected as the recipient of the 1999 URSI Koga Gold Medal. He was also the recipient of the UIUC 2001 Xerox Award for Faculty Research and appointed Beckman Fellow in its Center for Advanced Studies.